Photospheric observations of surface and body modes in solar magnetic pores

Keys, P. H., Morton, R. J., Jess, D. B., Verth, G., Grant, S. D. T., Mathioudakis, M., Mackay, D. H., Doyle, J. G., Christian, D. J., Keenan, F. P., & Erdelyi, R. (2018). Photospheric observations of surface and body modes in solar magnetic pores. *The Astrophysical Journal*, *857*(1), [28]. https://doi.org/10.3847/1538-4357/aab432

Published in:
The Astrophysical Journal

Document Version:
Publisher's PDF, also known as Version of record

Queen's University Belfast - Research Portal:
Link to publication record in Queen's University Belfast Research Portal

The Astrophysical Journal, 857:28 (15pp), 2018 April 10 https://doi.org/10.3847/1538-4357/aab432

Photospheric Observations of Surface and Body Modes in Solar Magnetic Pores

Peter H. Keys[1,2], Richard J. Morton[3], David B. Jess[4,5], Gary Verth[2], Samuel D. T. Grant[4], Mihalis Mathioudakis[4], Duncan H. Mackay[6], John G. Doyle[7], Damian J. Christian[5], Francis P. Keenan[4], and Robertus Erdélyi[2,8]
[1] Astrophysics Research Centre, School of Mathematics and Physics, Queen's University Belfast, Belfast, BT7 1NN, UK; p.keys@qub.ac.uk
[2] Solar Physics and Space Plasma Research Centre (SP^{2}RC), University of Sheffield, Hicks Building, Hounsfield Road, Sheffield, S3 7RH, UK
[3] Mathematics and Information Sciences, Northumbria University, Newcastle Upon Tyne, NE1 8ST, UK
[4] Astrophysics Research Centre, School of Mathematics and Physics, Queen's University, Belfast, BT7 1NN, UK
[5] Department of Physics and Astronomy, California State University Northridge, Northridge, CA 91330, USA
[6] School of Mathematics and Statistics, University of St Andrews, St Andrews, KY16 9SS, UK
[7] Armagh Observatory & Planetarium, College Hill, Armagh, BT61 9DG, UK
[8] Debrecen Heliophysical Observatory (DHO), Research Centre for Astronomy and Earth Sciences, Hungarian Academy of Sciences, 4010 Debrecen, P.O. Box 30, Hungary
Received 2018 January 10; revised 2018 March 1; accepted 2018 March 2; published 2018 April 10

Abstract

Over the past number of years, great strides have been made in identifying the various low-order magnetohydrodynamic wave modes observable in a number of magnetic structures found within the solar atmosphere. However, one aspect of these modes that has remained elusive, until now, is their designation as either surface or body modes. This property has significant implications for how these modes transfer energy from the waveguide to the surrounding plasma. Here, for the first time to our knowledge, we present conclusive, direct evidence of these wave characteristics in numerous pores that were observed to support sausage modes. As well as outlining methods to detect these modes in observations, we make estimates of the energies associated with each mode. We find surface modes more frequently in the data, as well as that surface modes appear to carry more energy than those displaying signatures of body modes. We find frequencies in the range of ∼2–12 mHz, with body modes as high as 11 mHz, but we do not find surface modes above 10 mHz. It is expected that the techniques we have applied will help researchers search for surface and body signatures in other modes and in differing structures from those presented here.

Key words: magnetic fields – magnetohydrodynamics (MHD) – Sun: activity – Sun: evolution – Sun: photosphere – Sun: oscillations

1. Introduction

The solar atmosphere is a highly dynamic magnetized plasma, whose structure is largely determined by the complex magnetic field that permeates through the layers. This gives rise to many of the features and phenomena frequently observed in the solar atmosphere. The advent of improved instrumentation and techniques has allowed many of their properties to be rigorously studied in recent years.

Undoubtedly, one of the most interesting aspects associated with the Sun's magnetic field, and which are frequently studied, are magnetohydrodynamic (MHD) wave phenomena. At their most basic, there are three possible MHD wave modes: the incompressible Alfvén wave, and the slow and fast magnetoacoustic waves (Goedbloed & Poedts 2004; Nakariakov & Verwichte 2005). Various wave modes have been observed across numerous features in the different layers of the solar atmosphere (see reviews by Banerjee et al. 2007; Wang 2011; De Moortel & Nakariakov 2012; Mathioudakis et al. 2013; Jess et al. 2015, to name a few). The Sun's convection zone excites a wide spectrum of global acoustic waves (*p*-modes), and when these interact with magnetic flux tubes embedded in the photosphere, they excite MHD wave modes with dominant periods of around 300 s (Braun et al. 1988; Sakurai et al. 1991). This MHD wave energy is then guided by the flux tubes to higher atmospheric layers. It is still not clear what happens to the upward-propagating wave energy, but there is evidence that *p*-modes play a pivotal role in governing the dynamics of the chromosphere, with shocks launching, e.g., chromospheric jets (De Pontieu et al. 2004). Furthermore, there are clear indications that the wave energy reaches the corona as, e.g., slow magnetoacoustic waves (De Pontieu et al. 2005; De Moortel 2009), or is transferred to transverse motions that could potentially play a role in heating the coronal volume (Morton et al. 2012, 2015; Freij et al. 2014; Grant et al. 2015, to name a few).

The foundation for the theoretical description of MHD waves in solar magnetic waveguide models, as it is widely used today, was formulated in the early 1980s in seminal papers by, e.g., Spruit (1982) and Edwin & Roberts (1983). Driven by observations, internal and external background quantities such as plasma density and magnetic field strength are allowed to vary, resulting in magnetic waveguides capable of supporting a much richer variety of MHD modes than are present in a homogeneous infinite plasma. This is most clearly seen from the dispersion diagrams of such waveguides, which display a complex variety of weakly and strongly dispersive magnetoacoustic wave modes, depending on, e.g., waveguide width, wavenumber, plasma beta, and internal/external Alfvén and sound speeds (Edwin & Roberts 1983). Also, the spatial structure of these wave modes is fundamentally determined by the cross-sectional shape of the waveguide. For example, a flux tube with circular cross section supports, e.g., azimuthally symmetric (sausage), asymmetric (kink), and higher-order perturbations (fluting modes). Another key property of such waveguides is whether the wave mode is evanescent in the external plasma, i.e., trapped by the waveguide, or oscillatory outside, i.e., leaky.

Often pores are employed to study sausage modes. Pores are relatively small (∼1–6 Mm in diameter) and have field

strengths of the order of a kilogauss (Sobotka 2003). Their small size means that they are more dynamic and responsive to external forces. Like sunspots, pores are darker than the quiescent solar surface. One study (Verma & Denker 2014) measured the mean intensity of a large sample of pores as being up to 40% below the surrounding surface, while more recent work (Dorotovič et al. 2016) on several pores using satellite data showed that they form when the intensity drops below 0.85 of the surrounding photospheric intensity value and the magnetic field increases to 650 G. Unlike sunspots, however, pores are devoid of penumbrae, meaning that they are fairly simple magnetic structures with lifetimes from several hours up to days (Sütterlin et al. 1996).

To observe sausage modes in ground-based data, several studies (Dorotovič et al. 2008; Grant et al. 2015; Moreels et al. 2015a; Freij et al. 2016) searched for oscillatory signals in the cross-sectional area and intensity of pores. A key conclusion in each of these works was that the fractional variations in both area and intensity were so minor that ground-based data were essential for studies of sausage modes in lower atmospheric regions. The first investigation of sausage modes (Aschwanden et al. 2004) observed them in large-scale loop oscillations in the corona, while the initial evidence of sausage modes lower in the atmosphere arrived several years later (Dorotovič et al. 2008) by analyzing white-light channels with the Swedish Solar Telescope. However, the latter authors only searched for oscillatory signals in cross-sectional area and not concurrent intensity oscillations. Subsequent work by Morton et al. (2011) conducted a more thorough investigation, looking for signals in both area and intensity oscillations in a blue continuum (4170 Å) channel, finding periods from 30 to 450 s. These authors noted that these periods would suggest that excitation of the sausage modes was due to global p-mode oscillations, and they also stated that the modes did not have large-amplitude wave power, provided that there were no twists in the magnetic field. A study of phase relationships between the area and intensity signals by Moreels et al. (2013) highlights that these signals are always in phase for slow modes, while they are in antiphase for fast modes. Moreels et al. (2013) suggest that Morton et al. (2011) observe the fast sausage mode. Dorotovič et al. (2014) studied both pores and sunspots for signatures of sausage modes and report both slow and fast modes, with periods ranging from 4 to 65 minutes. These results indicate that sausage modes can be excited in a range of photospheric structures of varying size and shape.

Observations of sausage modes in the chromosphere followed their discovery in the photosphere (Morton et al. 2012). Here the authors find kink and sausage modes in chromospheric fibrils, estimate associated energies of 11,000 W m^{-2}, and also that the modes were leaky. Therefore, it is possible for these modes to dissipate energy in the corona. Grant et al. (2015) employed multiple passbands and instruments to observe an upwardly propagating sausage mode from the lower photosphere to the upper photosphere/low chromosphere. They used the energy equations of Moreels et al. (2015b) to determine that the energy carried by the modes decreases substantially with height and, thus, may release significant energy into the surrounding chromospheric plasma. A recent study of two pores (Freij et al. 2016) using magnetoseismology techniques suggested that sausage modes in pores can be standing harmonics, with strong reflection at the transition region, indicating a chromospheric resonator.

One aspect of magnetoacoustic modes that has been predicted in theoretical work (Edwin & Roberts 1983), yet has been neglected in observational studies until now, is the wave character of the modes, i.e., whether they can be classified as surface or body modes. Expressed simply, a surface or a body mode can form at an interface where physical properties vary sharply and are analogous to seismic waves associated with earthquakes that occur at many tectonic plate boundaries on Earth. As properties such as magnetic field and density vary rapidly from a pore to its surroundings, pores should support surface and body modes. Recent theoretical work (Yu et al. 2017a, 2017b) showed that resonant damping of slow surface sausage modes could be efficient under conditions usually observed in pores. Some previous studies of pore oscillations (Grant et al. 2015; Moreels et al. 2015a; Freij et al. 2016) infer the surface/body characteristics of sausage modes using a combination of semiempirical models, theory, and the derived parameters of the modes from observations. Understanding the surface and body properties, however, is crucial in determining how energy is dissipated by modes in higher regions (Yu et al. 2017b). Here, for the first time to our knowledge, we present conclusive, direct evidence for the existence of surface and body modes in photospheric pores supporting sausage modes.

2. Theory Applicable to Sausage Modes

Most of the theory applicable to waves observed in solar pores has been derived previously (Spruit 1982; Edwin & Roberts 1983), employing, e.g., thin flux tube approximations. In our case, the thin-tube approximation is not applicable, and we must take the finite tube equations into consideration. We do not consider the effects of gravity on propagation here, though it may be important for pores found in the photosphere.

MHD modes that can propagate in a flux tube, such as a pore, under photospheric conditions fall into three distinct bands in terms of phase speed: fast surface modes, slow body modes, and slow surface modes. The phase speed for the slow modes is defined by the tube speed (c_T), and since the wave will be barely dispersive, it is given by

$$c_T = \frac{c_s v_A}{(c_s^2 + v_A^2)^{1/2}}, \tag{1}$$

where c_s is the sound speed and v_A is the Alfvén speed. The sound and Alfvén speeds are defined as

$$c_s = \sqrt{\frac{\gamma RT}{\mu}} \tag{2}$$

$$v_A = \frac{B_z}{\sqrt{\mu_0 \rho}}, \tag{3}$$

respectively, where γ is the ratio of specific heats, R the gas constant, T the temperature in the pore, μ the mean molecular weight, B_z the magnetic field component in the z-direction, μ_0 the magnetic permeability, and ρ the local plasma density.

Slow modes can be further divided into various angular modes, where $m = 0$ denotes the axisymmetric sausage mode in a cylindrical flux tube. The linear theory for sausage modes in a gravitationally stratified atmosphere has previously been studied in a rigorous manner (Defouw 1976; Roberts & Webb 1978; Díaz & Roberts 2006; Luna-Cardozo et al. 2012).

Consider a cylindrical waveguide with vertical background magnetic field denoted as $\boldsymbol{B}_0 = B_0\hat{z}$ and a velocity perturbation given by $\boldsymbol{v}_1 = (v_r, v_\theta, v_z)$. In the case of sausage modes, where $m = 0$, the equations for v_r and v_z decouple from the governing equation of v_θ. Hence, the magnetoacoustic modes will be described by v_r and v_z, while the Alfvén mode is given by v_θ. We are only interested in the magnetoacoustic mode, and we can therefore ignore the v_θ component and also that of the magnetic field in the θ-direction.

Surface and body modes are characterized by the spatial distribution of the amplitude across the flux tube (Rae & Roberts 1983; Zhugzhda et al. 2000; Erdélyi & Fedun 2010). The maximum amplitude for the surface mode will always occur at the boundary of the flux tube at the sharp discontinuity between the varying physical parameters of the equilibrium. For the body mode, the position of the maximum amplitude is dependent on the mode, i.e., the number of nodes in the *radial* direction, and the perturbed quantity chosen.

Equations for the amplitude of the internal plasma parameters for the sausage body mode (following Spruit 1982) are

$$v_z \propto J_0(mkr), \tag{4}$$

$$v_r \propto \frac{dJ_0(mkr)}{dr}, \tag{5}$$

$$b_z \propto v_z, \tag{6}$$

$$b_r \propto v_r, \tag{7}$$

$$p_1 \propto v_z, \tag{8}$$

where the Fourier-analyzed perturbations are assumed to have the form $f_1 \sim \exp(i(kz - \omega t))$. In the equations above, p_1 is the perturbation in the kinetic gas pressure and b is the perturbed magnetic field. Also, J_0 is the Bessel function of zeroth order and

$$m^2 = \frac{(v_A^2 - c_{ph}^2)(c_s^2 - c_{ph}^2)}{(v_A^2 + c_{ph}^2)(c_T^2 - c_{ph}^2)}. \tag{9}$$

Here c_{ph} is the phase speed of the mode. Note that these relations do not show the phase relations between the different variables under consideration. Taking into account these equations, we can conclude that v_z, b_z, and p_1 have maximum amplitudes at the center of the flux tube, while v_r and b_r are found to have maximum amplitude at the tube boundary. For higher harmonics in the radial direction, there may be nodes between the axis of symmetry and the boundary of the flux tube.

In the case of surface modes, the Bessel functions are replaced by the modified Bessel function, $I_0(n_0 kr)$, where $-n_0^2 = m^2 < 0$. Here all perturbations have a maximum at the tube boundary and are zero at the center of the tube. This behavior is demonstrated in the schematic shown in Figure 1 and shows how one would expect the power plots to look under the ideal scenario for both the body and the surface sausage modes.[9]

[9] Further visualizations of sausage modes in various simple geometries can be seen at http://swat.group.shef.ac.uk/fluxtube.html.

2.1. Predicting Surface/Body Modes

The value m^2 defined by Equation (9) in the previous subsection can be used to predict semiempirically whether we observe a surface or body mode, depending on whether it is positive or negative in value. To make this estimate, we use a combination of the observed physical properties available in our data sets, with some estimates for other parameters from models (Vernazza et al. 1981; Maltby et al. 1986) to estimate m^2 for each oscillation found in each data set.

It is clear from Equation (9) that to calculate m^2 we first must estimate the phase speed, c_{ph}. Here we only employ one bandpass in our analysis. Therefore, we utilize a technique demonstrated previously (Grant et al. 2015; Moreels et al. 2015b) to yield accurate estimates of the phase speed of a sausage mode oscillation using the equation

$$c_{ph} = c_s \sqrt{\frac{\pm A_m - 1}{\pm A_m - 1 + (\gamma - 1)\left(\frac{h\nu}{k_B T}\right)}}, \tag{10}$$

where h is the Planck constant, ν the frequency of the filter used in our observations, k_B the Boltzmann constant, and A_m the dimensionless amplitude. Note that the $\pm$ in the formula arises as this expression originates for a quadratic equation. The dimensionless amplitude, A_m, can be defined as

$$A_m = \frac{\delta I / I_0}{\delta A / A_0}. \tag{11}$$

Here δI is the amplitude of the intensity perturbation, I_0 the mean intensity, δA the amplitude of the area perturbation, and A_0 the mean area, all of which can be obtained from our observations. This approach of predicting whether a sausage mode is a surface or body mode has been performed previously (Grant et al. 2015; Moreels et al. 2015a). Now, we determine how accurate the method is with respect to our direct detection methods.

3. Observational Data

In total we employed seven data sets of various pores at disk center from 2011 to 2014. All were acquired with the Rapid Oscillations in the Solar Atmosphere (Jess et al. 2010, ROSA) instrument. ROSA is a multichannel broadband imager installed as a common-user instrument at the Dunn Solar Telescope (DST), New Mexico.

In this study, we employed the G-band continuum filter centered at 4305.5 Å with a bandpass of 9.2 Å with ROSA. This filter allows us to obtain photospheric intensity images at an estimated continuum formation height of ~100 km (Jess et al. 2012) and a theoretical 2-pixel, diffraction-limited resolution of $0\farcs14$ (~102 km) at a frame rate of 30.3 s^{-1}.

Localized seeing-induced wavefront deformations are corrected in the data in situ with the use of high-order adaptive optics systems (Rimmele 2004). However, this does not completely correct image deformations, and as a result, we must employ post facto image reconstruction techniques, such as the KISIP speckle interferometry package (Wöger et al. 2008), to obtain science-ready images. By utilizing 64 → 1 restorations, our reconstructed image cadence was increased from 0.033 to 2.112 s.

In tandem with ROSA, we employ line-of-sight (LOS) magnetograms for all data sets using observations from the

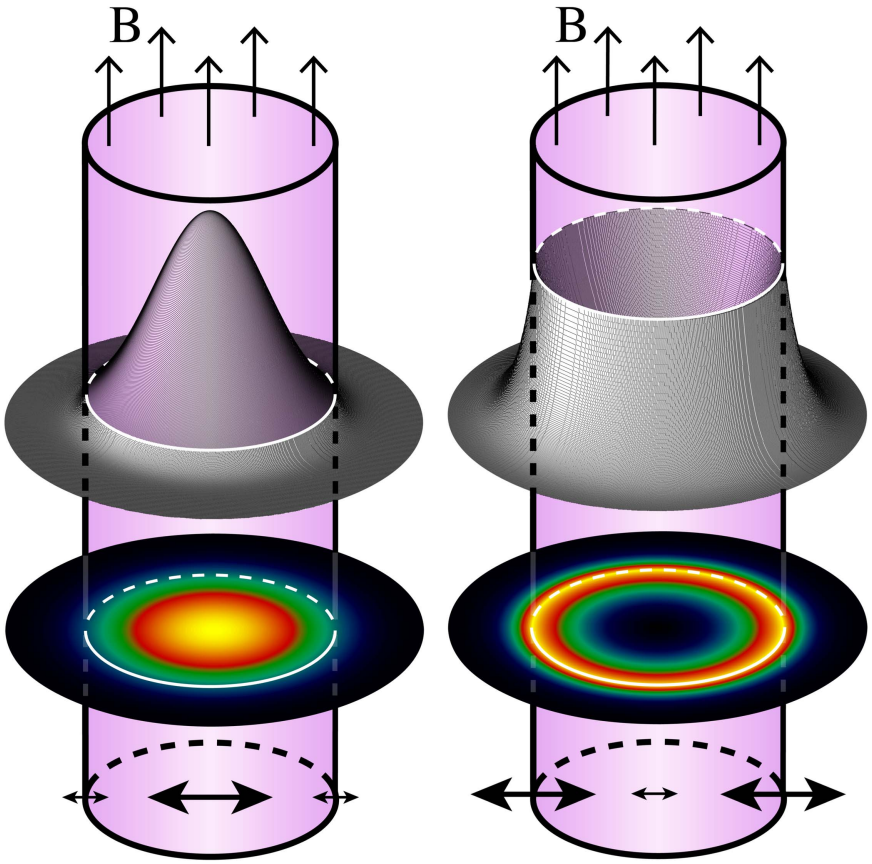

Figure 1. Simplified representation of magnetic flux tubes, with the arrows at the top indicating the magnetic field, ***B***. Plasma parameters (e.g., magnetic field, density) of the internal and external plasma differ. Magnetic flux tubes that support the MHD sausage mode are subject to a periodic variation in pressure and area (with these oscillations depicted by the arrows at the bottom). The surface plots (upper images) demonstrate the spatial structure of the pressure perturbation amplitude, which can have two distinct distributions. The amplitude of the body mode (left) is maximal at the central, inner part of the flux tube, with the power decaying close to the boundary. On the other hand, surface modes (right) are maximal at the tube boundary defined by the sharp changes in equilibrium quantities modeled as a discontinuity. The two-dimensional projection of the power is also demonstrated by the colored disks and can be compared to the observed distributions.

Helioseismic Magnetic Imager (HMI; Schou et al. 2012) instrument on board the *Solar Dynamics Observatory* (*SDO*; Pesnell et al. 2012). These data ensure that we have magnetic field information to establish estimates for values described in Section 2. Subsequently, the ROSA and HMI images needed to be aligned. To do this, we acquired both the HMI continuum images and the magnetograms for the corresponding times of the ROSA observations, and we prepared the data using the standard "*hmi_prep*" routine supplied by the *SDO* science team. For data alignment, we took a subfield of the HMI continuum images that represents the telescope pointing for each data set and degraded the ROSA images to match the resolution of HMI. We then employed Fourier cross-correlation techniques between the HMI continuum subfields and the degraded ROSA images to obtain accurate co-alignments. This process resulted in subpixel co-alignment between the HMI images and the degraded ROSA images, with maximum x- and y-displacements less than $1/10$ of an HMI pixel. Following such an accurate co-alignment, we could then construct the corresponding subfields for the HMI magnetograms for each data set. Note that the subsequent data analysis was performed on the nondegraded ROSA images.

In selecting data for analysis from the ROSA archive, we impose several criteria:

1. The data duration is greater than 20 minutes. This ensured that there is adequate sampling of any waves present, i.e., the data set is at least four times longer than the 5-minute frequency often associated with the p-mode spectrum.
2. The 2-pixel spatial resolution is better than $0\farcs5$. Due to the fractional area variations associated with sausage modes, we required good spatial sampling of pores. We estimate the spatial resolution using techniques described in Beck et al. (2007).
3. The cadence of the reduced data had to be shorter than 5 s. This ensures adequate temporal resolution in analyzing pore boundary variations and in determining subsequent oscillations with both wavelet analysis and empirical mode decomposition.
4. The pore data are close to disk center. This removes any LOS effects on boundary/intensity estimates induced by studying pores significantly away from disk center.
5. The pore data sets were acquired within the operational time frame of the *SDO*, i.e., after 2010 February. This ensures that there is adequate magnetic field information from the HMI instrument on board *SDO*.
6. The quality of the data sets, with regard to seeing conditions, is consistent. This ensures a more accurate determination of area and intensity oscillations. If the data contained patches of poor seeing, the resultant area and intensity measurements would result in inaccurate estimations of oscillation periods.
7. We limited the study to simple pores, i.e., we ignored pores with any developing penumbral elements or pores

Table 1
Summary of Observations for the Sample of Pores Studied

Data Set	Spatial Sampling	Resolution	Pointing	Sequence Duration (minutes)
2011 Jul 11	0.″069	0.″16	S16.3, E03.3	115
2011 Dec 09	0.″069	0.″17	N08.8, E10.0	75
2011 Dec 10	0.″069	0.″21	N07.6, W04.2	118
2012 Sep 30	0.″0935	0.″20	S06.7, E00.4	30
2013 Mar 06	0.″138	0.″30	S17.3, W07.0	35
2013 Aug 17	0.″069	0.″16	N17.5, E08.6	46
2014 Apr 15	0.″069	0.″17	S08.9, E04.6	51

with more complex structuring, e.g., pores separated by light bridges. By excluding pores with any penumbral elements, there will be less inclination in the magnetic field of the pore. This could possibly affect the analysis of the spatial structuring of the power within the pore and, as such, affect our determination of surface or body modes in the pore. We employed the HMI images to help isolate less complex pores by using the images to determine structures within the same flux concentration. This was used to determine if neighboring pores are actually separate entities, or if a more complex structure (such as a light bridge) exists within the data. By ignoring pores with more complex structures, one removes complex structures that may exhibit complex oscillatory phenomena, e.g., higher-order standing modes or mixing of modes. If this were the case, then the determination of the spatial structuring of the power would be more difficult, which is essential in determining whether a surface or body mode is observed.

These criteria isolated the seven data sets we study in this paper taken between 2011 and 2014. Table 1 summarizes the main characteristics of all data sets used in this study. An example image of each data set is shown in Figure 8 in Appendix A.

4. Analysis and Results

4.1. Wave Signatures and Mode Identification

To determine whether the signatures of sausage modes are present in our data, a time series of the area and intensity signals for the pores in each data set is calculated. We define the pore boundary as being any pixel 3σ below the mean value of intensity, which is calculated frame to frame utilizing a quiet region of the field of view (FOV) devoid of network magnetic bright points (MBPs) or the influence of the pore. The boundary is calculated within a box containing the pore under investigation to remove the possibility of counting other pores within the FOV in the area/intensity calculations. Once the pore boundary is established, the area and intensity within the boundary in each frame produce a time series of the variations in these properties over the duration of the data set for the pore. Concurrently, a time-averaged pore boundary map is created to subsequently identify the pore boundary location when determining the spatial properties of the mode later in the analysis.

Wavelets are employed here, as they are considered a standard tool for studying periodic oscillations in signals (Torrence & Compo 1998; Grinsted et al. 2004). In comparison to traditional Fourier methods, where the basis functions are localized only in the frequency domain, wavelet analysis methods are localized in both the frequency and time domains so that the signal is decomposed into both the frequency and time space simultaneously. This allows information to be obtained on both the amplitude of periodic signals and how this amplitude varies over the duration of the signal. In our wavelet analysis we use the 99% significance level to establish that the periods are real. We use wavelets in the first instance to search for oscillatory signals in both the established area and intensity signals.

Empirical mode decomposition (EMD) is a key part of the Hilbert-Huang transform (Huang et al. 1998; Terradas et al. 2004; Huang & Wu 2008), which we employ here as a complementary technique to wavelet analysis. It is a powerful statistical tool that decomposes a signal into its intrinsic timescales. The components are finite in number and are referred to as intrinsic mode functions (IMFs). Decomposition of a signal into its composite IMFs is useful in analyzing both nonstationary and nonlinear signals, as the decomposition is based on the local characteristic timescale of the data (i.e., without leaving the time domain). EMD is useful in overcoming some of the limitations of wavelet analysis such as leakage and low time-frequency resolution, which makes it an attractive tool for MHD wave studies.

Each IMF has its own timescale of variation with oscillations symmetric about the local zero mean. As such, the IMF is a function where the number of extrema and zero crossings for each IMF must either be equal or differ, at most, by one. Also, at any point in the IMF, the mean value of the envelope defined by the local maxima and the envelope defined by the local minima must be zero. The first condition reduces period mixing by ensuring that wildly varying periods are not included within the same IMF, while the second condition maintains the local requirement that the oscillations are about zero.

Utilizing these time series and wave identification techniques, the dominant periods within each data set for both the intensity and area are obtained (Figure 2), with both signals displaying significant power, with periodicities in the range of 90–700 s. The most common oscillations detected for the two variables, namely, intensity and area, have periods $\sim 300 \pm 45$ s, consistent with the idea that these waves are excited by the absorption of *p*-modes. The final column of Figure 8 in Appendix A shows the power as a function of frequency for the pores studied. The frequencies of highest power fall within the range of ~2–5 mHz, which is consistent with the range of frequencies associated with the *p*-mode spectrum (see Figure 2 of Ludwig et al. 2009). This is further evidence that the wave modes are driven by *p*-modes. However, the detected wave power is not continuous and reveals that the waves are composed of coherent wave trains of short duration (Figures 2(c) and 3). Such behavior has also previously been identified in sunspot waves (Bogdan & Judge 2006). Corresponding perturbations in the magnetic field in HMI data were not found, likely due to the

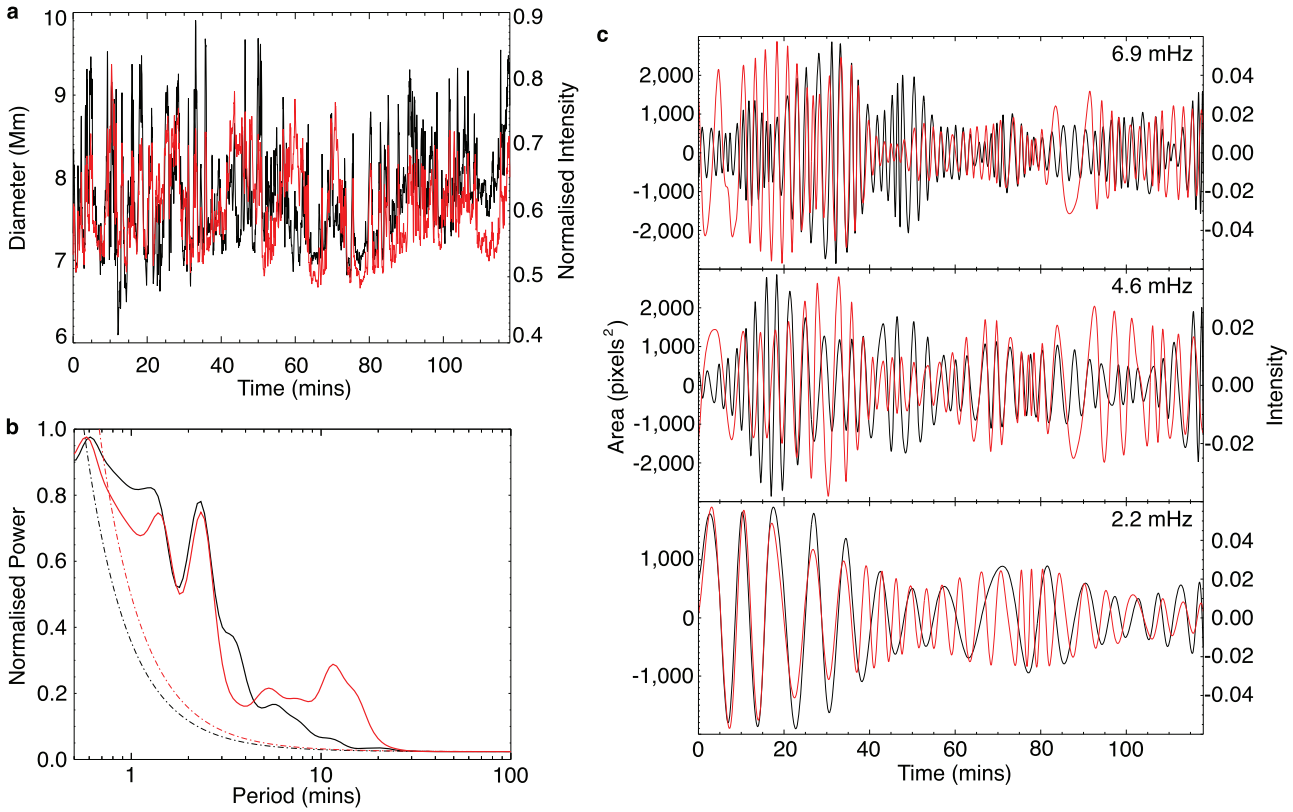

Figure 2. Multiple techniques are employed to determine oscillatory signals present in our data before filtering to observe the spatial distribution of the power. Panel (a) is the area (black) and intensity (red) signals established for a single pore over the duration of the observation sequence (2011 December 10 data set). Panel (b) shows the dominant periods as determined by employing wavelet analysis on both the area and intensity signals, with the dashed lines indicating the 99% significance levels. Panel (c) shows the result of employing the complementary EMD technique on the area and intensity signals in panel (a). IMFs at three different frequencies for both the area and intensity oscillations are displayed. This information is employed along with wavelet analysis to determine whether a sausage mode oscillation is present in the data, the dominant periods of oscillation, and whether the fast/slow sausage mode is observed.

expected magnetic field variation being of the order of the sensitivity of HMI (Grant et al. 2015).

To determine whether the observed oscillations are slow or fast MHD sausage modes, the phase relationship between the intensity and area signals of the pore is calculated. Due to the presence of discrete packets of oscillatory power, the time series is evidently not stationary. To accurately assess the cross-spectral phase in the presence of nonstationarity, two methods are employed. The first utilizes wavelets and determines the phase and the coherence by evaluating the cross-spectrum between the two signals, while the second exploits EMD, decomposing the signal into a finite number of IMFs. IMFs of the intensity and area time series with similar timescales are then compared for phase relations. These complementary techniques reveal that the intensity is in phase with the change in area of the pores when a wave packet is identified, suggesting that the observed wave behavior is the compressible slow sausage mode (Moreels et al. 2013).

Figure 2 shows the result of these various processes to determine the wave mode, where panel (a) plots the area (black) and intensity signals (red) for the duration of an observing sequence of a pore (2011 December 10 data set) obtained from the ROSA archive. Panel (b) displays the dominant periods as determined by employing wavelet analysis on both the area and intensity signals, with the dashed lines indicating the 99% significance levels, while panel (c) demonstrates the result of employing the complementary EMD technique on the area and intensity signals in pnael (a). The plots here are the IMFs at three different frequencies for both the area and intensity oscillations for this particular data set. Note that, as the waves are composed of coherent wave trains of short duration, the wave power is not continuous. This results in the observed area and intensity signals not being in phase for the whole duration of the time series as seen in the IMFs in Figure 2. Effectively the sausage modes are quasi-periodic as a result of the imperfect waveguides and drivers in the observed data. IMFs and wavelet analysis are used to determine the frames that are isolated to observe the spatial distribution of the power for these individual wave trains.

4.2. Spatial Distribution of Power

The novel aspect of this work is the determination of the spatial structure of oscillatory power. With confidence in the identification of the wave mode, we can now progress with the important objective of determining whether the oscillatory behavior displays the signatures of either the surface or body modes. The power distribution for both the surface and body modes depends on the azimuthal wave-mode number and the perturbed quantity examined. In Figure 1, we demonstrate the expected spatial distribution of power of the gas pressure for both the body and surface slow sausage modes (see Section 2 for more details). The kinetic gas pressure amplitude is shown, as this represents the variation in the key parameters that

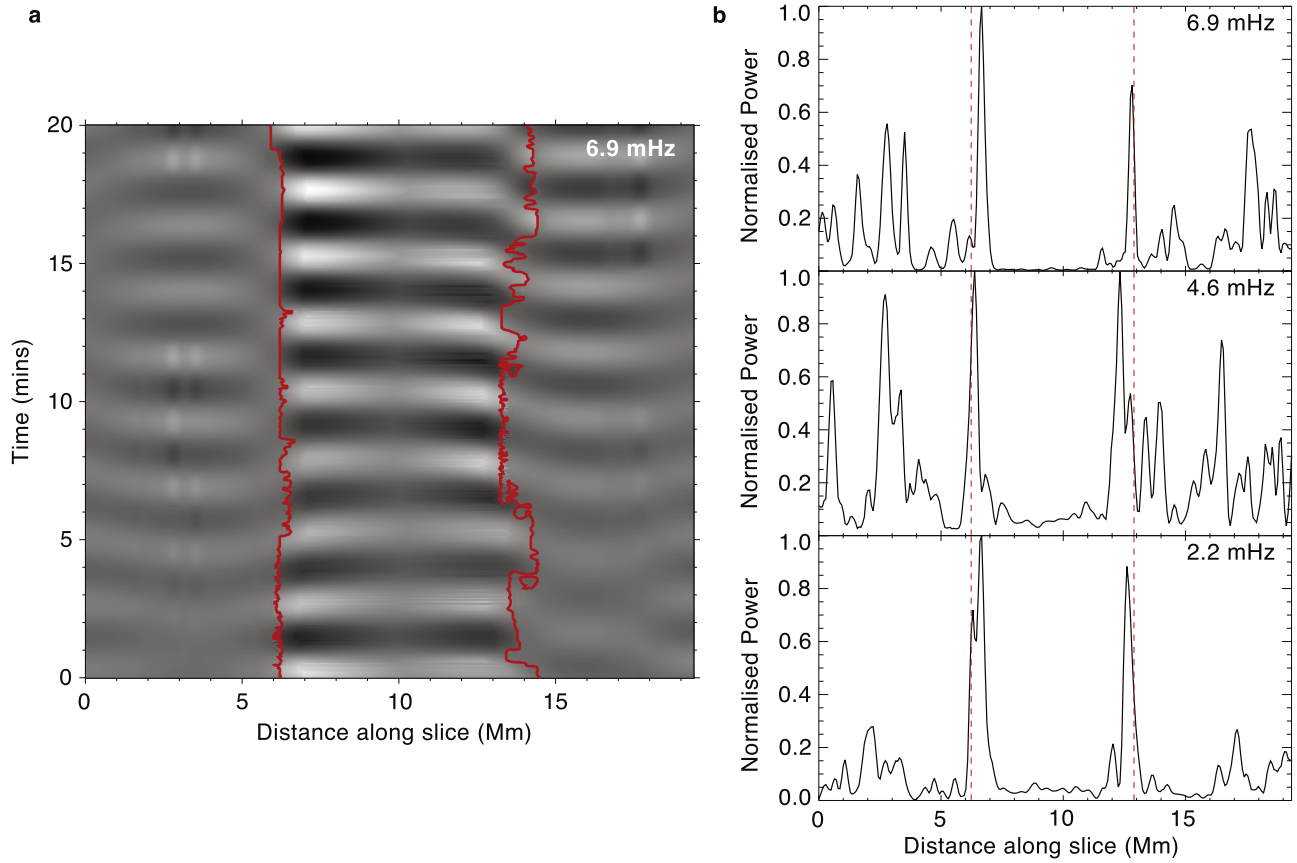

Figure 3. Coherent oscillatory behavior is identified throughout the pore for data from 2011 December 10 and is occurring with a number of distinct frequencies. Panel (a) shows a temporally filtered (at ∼6.9 mHz) time–distance diagram taken from a slice across the pore. The analysis reveals a clear, spatially coherent oscillatory pattern within the pore boundaries (outlined in red). The time axis of the plot is clipped to 20 minutes to ensure that the small pixel-to-pixel amplitude variations across the pore are evident. The time window is established by using EMD and wavelet analysis to determine when a clear in-phase wave is present in the filtered area and intensity signals (Figure 2). In the above plot, the 20-minute window equates to the time period of 35–55 minutes from the start of data acquisition and represents the time period over which the corresponding plot in panel (b) is derived. The right-hand panels display the normalized Fourier power for three distinct oscillatory frequencies of the pore. The power is seen to peak close to the temporally averaged location of the pore boundary (red dashed lines), supporting their characterization as a surface mode. Figure 4 indicates the cut used to make these plots and demonstrates the process of filtering light curves at both the pore boundary and pore center for the various oscillations present here.

govern the image intensity, i.e., gas temperature and density. It is evident that for the sausage body mode the peak power will generally be concentrated within the center of the waveguide, with the power decreasing toward the pore boundaries. On the other hand, the peak power of the surface sausage mode is located at the boundaries of the waveguide, decreasing to the center. For both modes, at least in homogeneous ambient plasmas, the external wave power should decrease exponentially as a function of distance from the pore boundary. We note that the schematic in Figure 1 is a visualization sketch, highlighting only the most basic features of surface and body modes. It should be expected (and is observed) that the physical picture is much more complex, with many factors likely contributing to the observed amplitude profile, e.g., radial structuring, variations in cross-sectional geometry, and time dependence due to plasma dynamics.

To analyze the distribution of power across the pore, the power is examined at selected frequencies for both one-dimensional cuts across the pore and two-dimensional power maps. The power for each frequency examined is averaged over sections of the time series where significant power was found from the wavelet/EMD analysis. Having determined prominent, periodic perturbations simultaneously between area and intensity signals in the data, the dominant oscillatory frequencies were isolated by applying Gaussian filters to the data. To do this, each pixel within the data set is treated as a time-varying light curve and converted to frequency space with a fast Fourier transform (FFT). This is then convolved with a Gaussian profile with a central frequency, f, corresponding to the frequency under investigation and a width given by $\pm f/10$ to ensure narrow frequency filtering. The filtered data are then converted back into the temporal domain with an FFT. Time–distance plots of the filtered data result in figures such as Figure 3(a). Using a combination of well-known wavelet and EMD techniques allows us to isolate the frames in the filtered data in which clear, in-phase oscillatory signals in both area and intensity are observed. Focusing on these frames alone allows us to evaluate the one-dimensional power plots (Figure 3(b)) across a range of angles around the pore, which can be used to determine the one-dimensional spatial distribution of power across the pore (see also Figure 8 in Appendix A for more examples).

Figure 4(a) depicts the location of the cross-cut used to create the plots in Figure 3. In this panel, a cross along the slice marks the pixel locations used for the subsequent plots displayed in panels (b) and (c), with one chosen to represent the pore boundary (green) and another to represent its center (red). Panel (b) is the collection of untouched light curves for

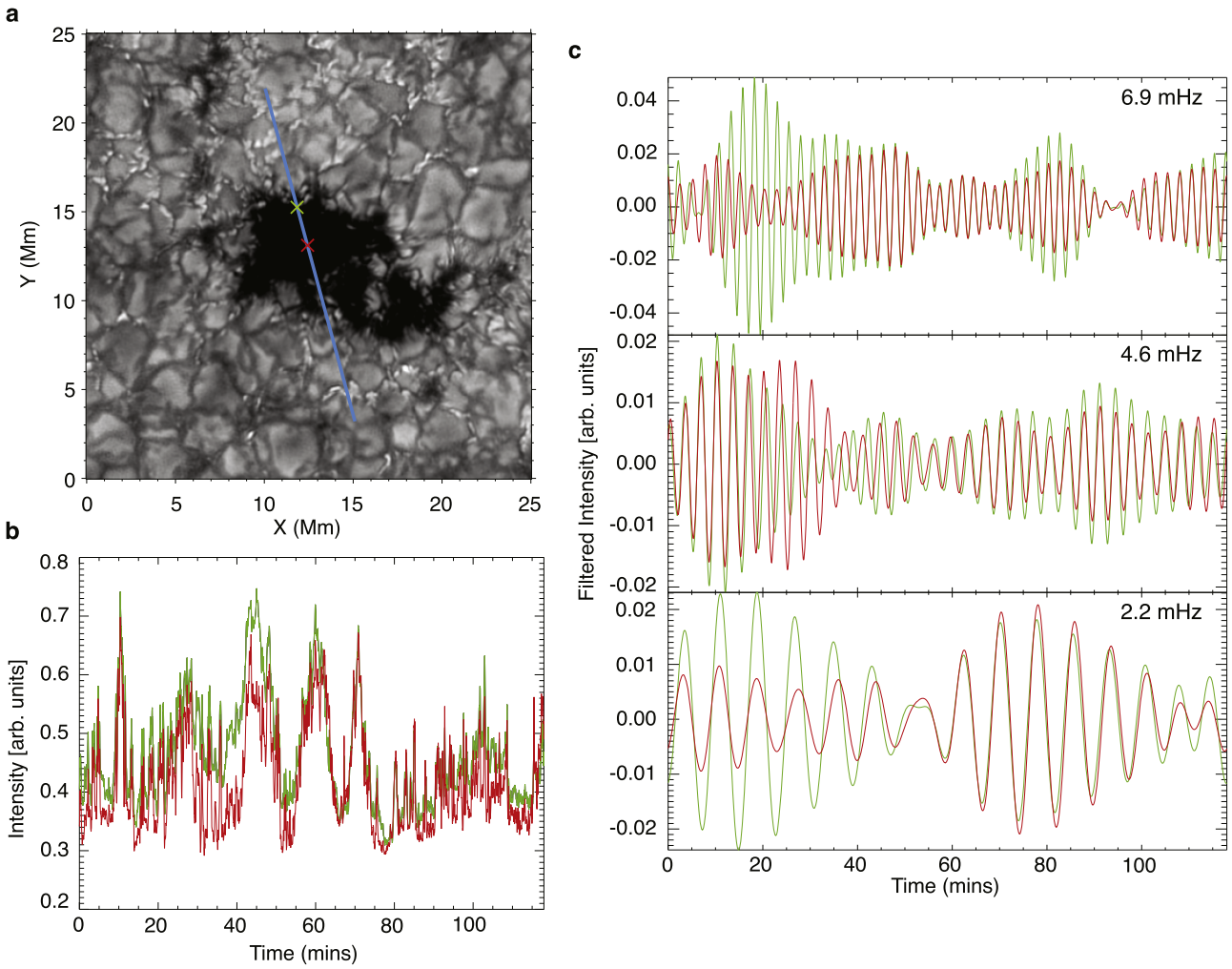

Figure 4. Panel (a) shows a subfield of the pore under analysis in Figure 2, with the blue line indicating the cross-cut used to make the images in Figure 3. The red and green crosses indicate the locations used to plot the subsequent light curves shown in panels (b) and (c) for a pixel at the center of the pore (red) and at the pore boundary (green). Panel (b) shows the unaltered intensity curves for these locations, with the color of the line consistent with the crosses in the panel above. Panel (c) shows the results of filtering these light curves as described in the main text over the whole time sequence of the data set. Again, the colors of the plots are consistent across all panels. It is clear from the filtered plots that there is significant amplitude in intensity oscillations at both the pore boundary and the interior across all three sampled frequencies. The power plots in Figure 3(b) of the main text are created using frames in the range of ∼35–65 minutes, ∼66–84 minutes, and ∼1–29 minutes from the start of the observing sequence for the 6.9, 4.6, and 2.2 mHz oscillations, respectively.

these two locations (with the colors used matching the crosses in panel (a), while panel (c) is the result of filtering the light curves for the three Gaussian filters used for this particular data set. It is clear from the filtered plots that there is significant amplitude in intensity oscillations at both the pore boundary and the interior across all three sampled frequencies. The power plots in Figure 3(b) are created using frames in the range of ∼35–65 minutes, ∼66–84 minutes, and ∼1–29 minutes from the start of the observing sequence for the 6.9, 4.6, and 2.2 mHz oscillations, respectively.

Isolating the frames, in which the oscillation is dominant, is key, as it allows the spatial characteristics of the wave mode to be determined more readily. Establishing the power at each pixel within these isolated frames was performed with both Fourier and wavelet techniques. Again, each pixel of the filtered data was treated as an individual light curve with the power calculated as the absolute value of the FFT/wavelet squared. This procedure resulted in two-dimensional power plots (Figure 5) showing the spatial distribution of the power, hence revealing whether a surface or body mode is observed. One-dimensional cross-cuts of these power maps produce the power profiles displayed in Figures 3(b), 5(b), and 8.

The filtered time–distance diagrams reveal that the pores have coherent in-phase oscillations across their entire structure (Figure 3(a)). Significantly, this result highlights that the entire pore can be excited coherently, acting effectively as a monolithic magnetic flux tube. This is different from the wave behavior of the larger sunspots, which apparently do not show signatures of being excited as a single object. As such, there is no evidence in any of the pores here for the distinct "nested bowl" routinely observed in sunspot oscillations (Rouppe van der Voort et al. 2003). This is probably the result of the dominant oscillations of the pores studied being globally excited, whereas in the case of sunspots, only a portion of the sunspot is excited, leading to the chevron structures in filtered time–distance cross-cuts. It is possible that the difference in physical scales between pores and sunspots is responsible for the visible wave excitation signatures, with the relatively smaller spatial size of pores allowing the underlying wave drivers to globally excite the observed waves.

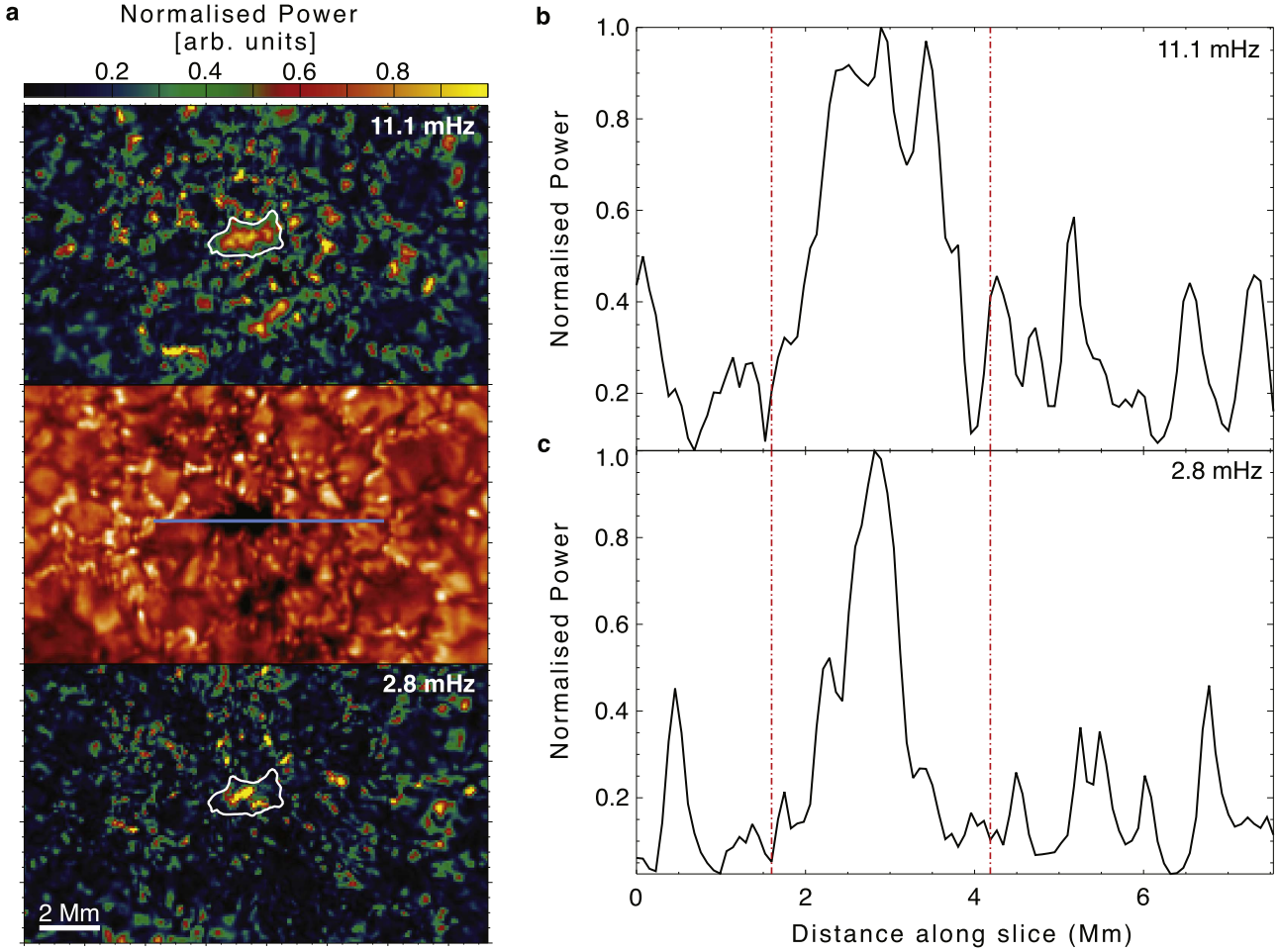

Figure 5. The oscillatory signals of a near elliptical pore (central panel in (a)), observed on 2012 September 30, reveal concentrations of power peaking at the center of the pore. The upper and lower panels of (a) show the wavelet power for the pore filtered at a central frequency of 11.1 and 2.8 mHz, respectively. White contours in these power maps show the time-averaged boundary location for the pore. Images in (b) display the corresponding one-dimensional cross-cuts for the two power maps in (a). Cuts were taken from the position marked by the blue line in the central panel of (a). The red dashed lines in (b) indicate the pore boundary. Again, it is evident in these cross-cuts, as with the two-dimensional power plots, that power peaks within the center of the pore and decays at the boundaries, which is synonymous with the body mode.

The oscillatory behavior in the pore can also be contrasted with the signal in the surrounding granules. We observe significant power at periods of ∼300 s in the surrounding granulation, likely to result from *p*-mode leakage into the surrounding photosphere along small-scale or weak fields in the intergranular lanes (Braun et al. 1988; Li et al. 2001). It is evident that the oscillatory behavior outside of the pores does not display the same large-scale coherence observed within the pores. Rather, the perturbations appear more random with regard to their spatial distribution and phase. The striking fact that the pores are essentially excited as a monolithic structure opens up unique and exciting avenues for studying the behavior and nature of the oscillatory phenomenon.

It should also be noted here that it is possible that there is an enhancement of power due to small-scale reconnection at the pore boundary. However, we refute this possibility, in this case, owing to a number of reasons, such as the uniformity of power enhancement around the pores and the fact that the free energy is two orders of magnitude below the 1σ error estimate (i.e., the noise estimate) of the field energy. Full details of our reasoning are given in Appendix B.

4.3. Surface Waves

It is found that the surface wave is the dominant oscillatory mode excited, with signatures of the mode both present in all pores examined and visible across a wide range of frequencies. Figure 3 displays a sample of the obtained spatial distributions of power for a pore at a range of frequencies. It may be seen from the figures that the maximum of power in the pore occurs along the interface between magnetic and nonmagnetic regions, i.e., at the pore boundaries, and the power decreases to a minimum toward the center of the pore. A comparison with Figure 1 reveals that the observed distribution is strikingly similar to the sketch demonstrating the key features predicted by solar MHD wave theory for surface modes. The peak power is not precisely coincident with the time-averaged pore boundary, but this is not surprising since the size and location of the pore vary as a function of time, which will naturally influence the positions of the identified boundaries.

Figure 3(a) shows a time–distance cut of the filtered intensity, with the time axis limited to a 20-minute window in which the oscillation is clearly present as determined through both wavelet and EMD analyses. The corresponding power plot

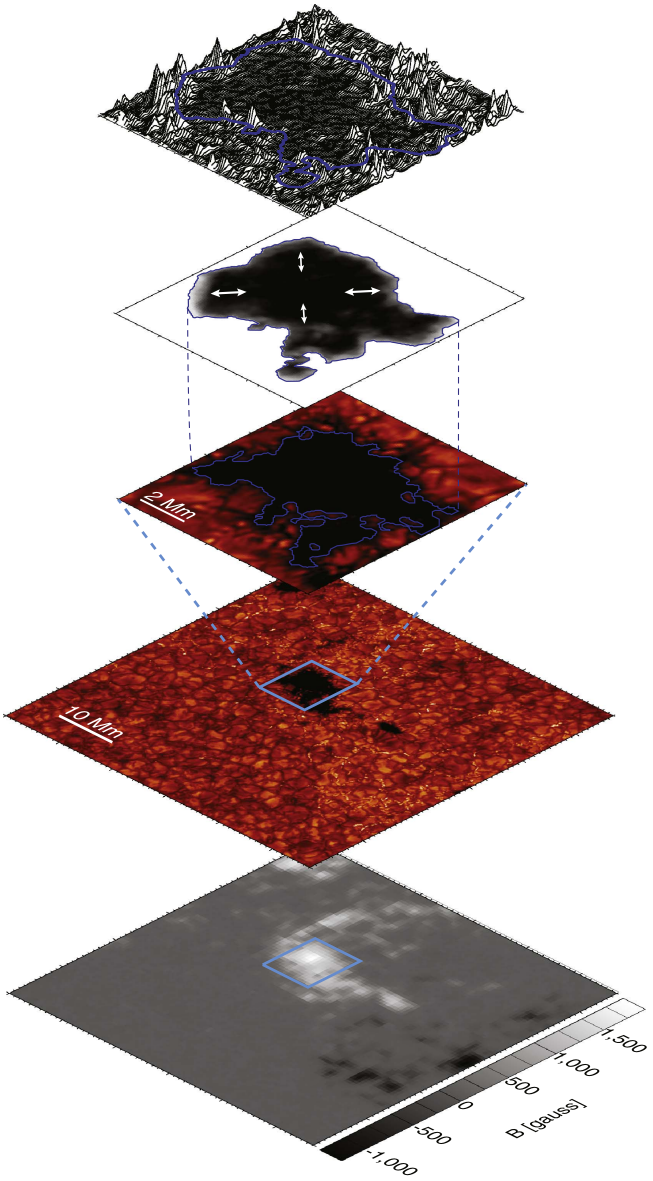

Figure 6. This stack image shows the basis of our designation of a sausage surface mode in this pore. The bottom panel shows the LOS magnetogram from HMI indicating the magnetic field of the pore and the sharp boundary in terms of magnetic field at the pore's edge. Above this is the full FOV ROSA G-band image showing the photospheric appearance of the pore taken on 2011 December 10. The blue box indicates the expanded region shown in the top three panels. The expanded G-band image has blue contours indicating the pore boundary established for that particular frame. Above this is the time-averaged pore boundary map showing the variation in boundary location during our observation sequence, where the arrows indicate the sausage mode oscillations present. The top panel is a two-dimensional power plot of the power across the pore obtained with wavelet transforms of the data filtered at a frequency of ∼4.6 mHz. The blue contour shows the time average pore boundary location. Peaks in power at this boundary indicate that a sausage mode is observed at this frequency.

in panel (b) is constructed using this window. Note that all of the power maps are generated for times within our observing sequences when the oscillation is clearly present, as opposed to the whole duration of the series, which would act to mask out the power signal of the oscillations. It is clear in the time–distance slice of Figure 3(a) that there is significant wave amplitude at the boundary of the waveguide, which manifests as peaks in power in the one-dimensional power plots. There is still some discernible intensity amplitude within the center of the pore, which is relatively weak and is not seen in the corresponding power plot. This may not be entirely unexpected, as it is possible that the pore has a steep gradient in density radially, which inhibits wave power within the pore. Figure 4 shows the cut used to produce the plots in Figure 3 and demonstrates this phenomenon by showing the variation in light curves observed at the pore boundary and at a central location for the sample pore. It is evident in this plot that there is discernible amplitude at the center of the pore in the filtered intensity plots. However, the amplitude of the oscillations is larger toward the boundaries.

In Figure 6, a two-dimensional surface plot of the power for a surface mode oscillation at 4.6 mHz is displayed. It is clear that the power of the oscillation peaks at the boundary of the pore, with significant reduction in power across its internal region. The magnitude of the power is not homogeneous around the boundary, likely due to longer-term variations in the pore boundary that will smear out the signal. In some examples, we observe relatively small power peaks within the pores. These peaks appear spatially consistent with the ingress of granules within our defined time-averaged pore boundary, during the evolution of the pores. In choosing pores for this study (see Section 3 for our selection criteria), we also opted to choose simple structures, e.g., by neglecting pores with noticeably complex structure, e.g., light bridges. These power peaks associated with the ingress of granulation highlight the need for simple structures for the identification of the wave modes. The observed spatial distribution of power is seen for the majority of pores analyzed, occurring for many frequencies over a wide range (see Figure 8 in Appendix A for examples). Full details of the oscillatory behavior found across all pores are given in Table 2.

4.4. Body Waves

From all the data sets examined, the distribution of power presented only two clear cases of the body mode (Figure 5), corresponding to data taken on 2012 September 30 and 2013 March 6. In both these data sets the body mode was observed unambiguously at the highest frequency (∼11 mHz). The distribution of power is observed to be maximal at the center of the pore and decreases toward the boundary (and, of course, away from the boundary similar to surfaces waves). Two-dimensional power plots are displayed in Figure 5(a), with the symmetry of the distribution of power clear at 11 mHz. The corresponding one-dimensional cross-cut supports this (Figure 5(b)), although it reveals that the observed signal is more complex than the simple schematic presented in Figure 1. For the oscillation at 2.8 mHz, there are two distinct concentrations of power within the center of the pore. This still conforms to the description of a body mode. However, it is not as clear-cut as the 11.1 mHz example. The two concentrations of power, in this instance, could be the result of a higher radial harmonic at that particular frequency, although as our examples of such a power distribution are limited, we can only speculate that this is the case here. The pore in this figure is seen to possess a highly elliptical cross-sectional geometry, but this does not affect the interpretation. It is thought that potentially any cross-sectional geometry of a waveguide will allow for the existence of both body and surface modes. In particular, sausage mode oscillations of both surface and body

Table 2
Summary of Observed/Predicted Parameters for Pores Studied

Pore Property	2011 Jul 11	2011 Dec 09	2011 Dec 10	2012 Sept 30	2013 Mar 06	2013 Aug 17	2014 Apr 15
$\|B\|$ (G)	1300	1200	1200	820	850	990	1100
Av. diameter (Mm)	8.6 ± 0.2	5.6 ± 0.3	7.7 ± 0.3	1.5 ± 0.1	1.3 ± 0.6	3.0 ± 0.8	6.3 ± 0.7
δ area (%)	1.61 ± 0.49	1.72 ± 0.62	4.01 ± 0.88	2.45 ± 0.42	2.80 ± 0.21	2.02 ± 0.65	2.22 ± 0.34
Av. intensity	0.43 ± 0.06	0.52 ± 0.03	0.60 ± 0.05	0.63 ± 0.06	0.59 ± 0.04	0.60 ± 0.02	0.49 ± 0.04
δ inten. (%)	1.47 ± 0.20	2.16 ± 0.34	2.10 ± 0.42	3.15 ± 0.19	1.90 ± 0.41	1.09 ± 0.39	2.54 ± 0.19
Observed freq. range (mHz)	2.0, 4.4, 9.5	2.1, 3.9, 7.4	2.2, 4.6, 6.9	2.8, 4.6, 11.1	3.6, 6.9, 11.8	2.5, 4.1, 7.1	2.9, 5.3, 10.0
Surface (S) or body (B) observed	S, S, S	S, S, S	S, S, S	B, Both, B	B, Both, B	S, S, S	S, S, S
Surface (S) or body (B) predicted	S, S, S	S, S, S	S, S, S	B, S, B	B, S, B	S, S, S	S, S, S
Average energy estimates (kW m^{-2})	43.4 ± 11.0	28.8 ± 14.7	6.2 ± 1.9	8.6 ± 4.8	8.5 ± 3.1	6.3 ± 0.8	41.1 ± 10.6

type have been theoretically demonstrated to be supported by elliptical waveguides (Erdélyi & Morton 2009).

The oscillatory signals observed within the data sets were also subject to a series of theoretical tests to predict the characteristics of the modes (see Section 2.1 for more details). Such tests involved the extraction of area and intensity information, which fed into a theoretical framework permitting the calculation of the phase velocity, which subsequently allowed us to predict the wave character. The model outputs displayed excellent agreement between the observed wave modes and those predicted by the theoretical method for the most part. Previous work (Grant et al. 2015; Moreels et al. 2015a; Freij et al. 2016) employed these methods as an indirect way for detecting slow surface modes, the results of which are in agreement with what we find here.

5. Concluding Remarks

We have demonstrated that magnetic pores are ideal features for studying the properties of MHD waves in solar magnetic waveguides. The pores harbor a wide range of oscillatory perturbations and appear to be excited as a monolithic structure. This behavior, along with their large size, enables the radial spatial structure of the oscillatory modes to be probed. The wave behavior displays amplitude distributions that are in agreement with those predicted from theoretical models (Spruit 1982; Edwin & Roberts 1983), although, as to be expected, the physical properties of real pores (e.g., geometry) and the surrounding atmosphere cause deviations from the simplified theory. However, the evidence presented here demonstrates in a compelling way that body and surface modes naturally exist in the Sun's atmosphere.

For the relatively small sample of pores, we found that the surface mode is more prevalent than the body mode. At present, it is unclear as to why the surface mode dominates the excited oscillatory signals. Considering all the derived parameters for the pores (Table 2), the only relationship between the pore parameters and modes present is the size and/or strength of LOS magnetic field. For our limited sample, we observe that for pores with diameters less than about 3 Mm and field strengths below about a kilogauss, the body modes are present. It is likely that the stronger field strength results in a sharper gradient between the pore and the quiescent environment, which allows the surface mode to be more readily supported in the pore. More research would need to be undertaken to clarify this.

It has also been suggested that pores can support a significant amount of wave energy (Grant et al. 2015), with the potential to power the local dynamics of the lower solar atmosphere. Utilizing the theoretical framework for energy flux estimates (Moreels et al. 2015b), we suggest that at the photospheric level the surface modes transport at least twice the energy (22 ± 10 kW m^{-2}) as the observed body modes (11 ± 5 kW m^{-2}). This may be significant in determining which mode contributes more to localized atmospheric heating as a function of waveguide height. Again, more work needs to be done to clarify this in the context of energy deposition with height.

The ability to observe the radial spatial structuring of pores will also open up new avenues in MHD wave studies. In particular, the use of solar magnetoseismology to probe the local plasma conditions is expected to allow significant progress. We envisage that advanced models of magnetic flux concentrations embedded in a convective plasma, used in conjunction with current and further observations, will further improve our understanding of the complex physics and wave behavior that is observed within this study.

P.H.K. and R.J.M. are grateful to the Leverhulme Trust for the award of Early Career Fellowships. D.B.J. wishes to thank the UK Science and Technology Facilities Council (STFC) for the award of an Ernest Rutherford Fellowship alongside a dedicated Research Grant. D.B.J. and S.D.T.G. also wish to thank Invest NI and Randox Laboratories Ltd. for the award of a Research & Development Grant (059RDEN-1) that allowed this work to be undertaken. M.M. and F.P.K. acknowledge support from the STFC Consolidated Grant to Queen's University Belfast. R.E. acknowledges the support received from the Royal Society. Armagh Observatory is funded by the Northern Ireland Department of Communities. Observations were obtained at the National Solar Observatory, operated by the Association of Universities for Research in Astronomy, Inc. (AURA), under cooperative agreement with the National Science Foundation. Two data sets (2013-08-17 and 2014-04-15) were acquired within the SolarNet Project. SolarNet is a project supported by the EU-FP7 under grant agreement 312495. The authors wish to thank the DST staff and Dr. Gianna Cauzzi for help in acquiring data.

Appendix A
The Viability of G-band for the Analysis

We employed G-band in the analysis for a number of reasons. As a continuum filter, we expect that there will be a relation between the intensity of the image and temperature to some extent. This is evident when looking at MBPs in G-band

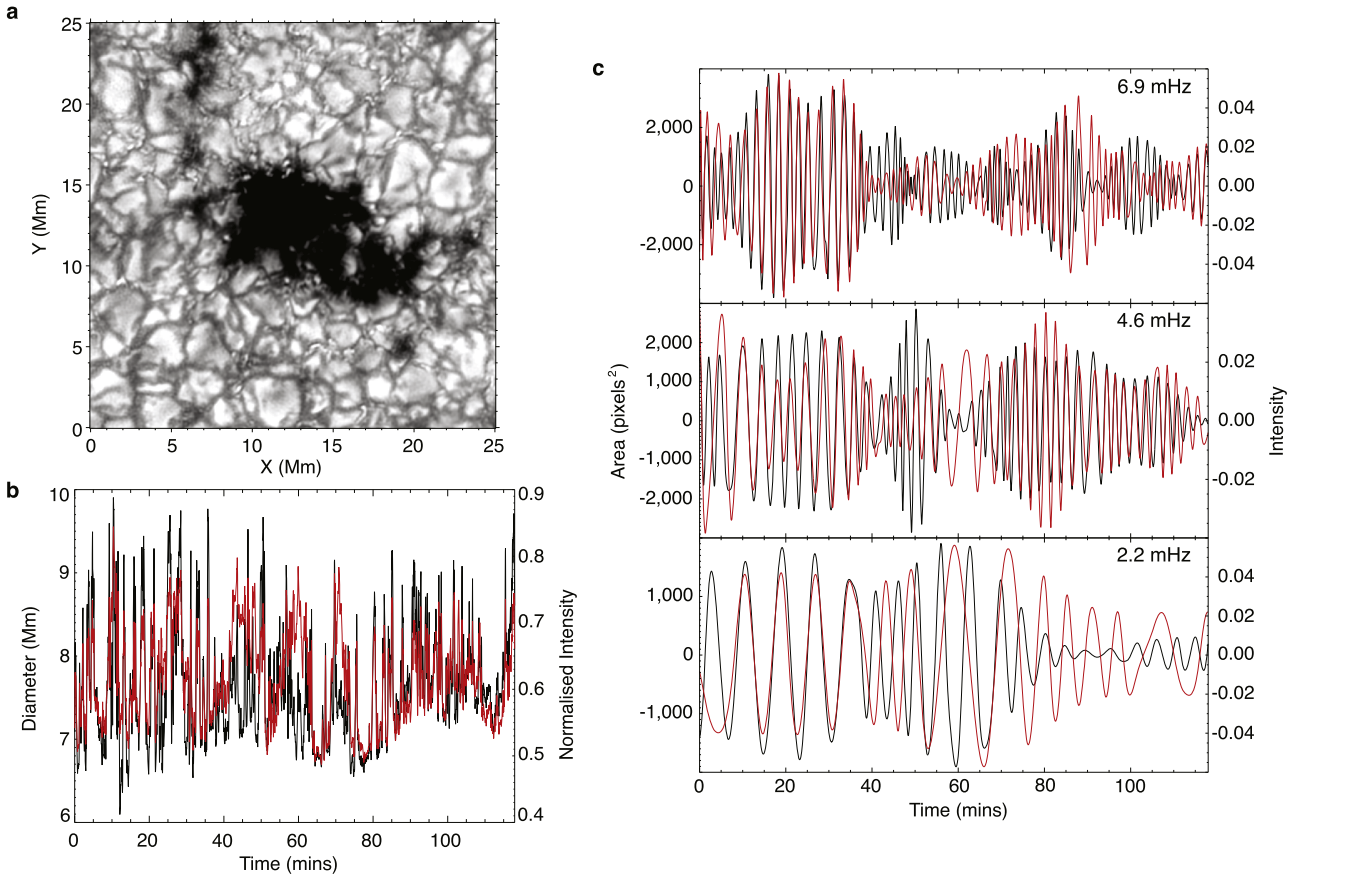

Figure 7. The images presented here help to verify the decision that the G-band continuum filter is an acceptable continuum bandpass for studying sausage oscillations in photospheric pores. Panel (a) shows a subfield of data taken with the 4170 Å continuum filter for the 2011 December 10 data set used in the paper. This is the same subfield as depicted in Figure 4. Panel (a) shows the visual similarities between the two filters. Panels (b) and (c) mirror plots seen in Figure 2. Panel (b) shows the area (black) and intensity (red) signals for the pore over the duration of the observing sequence for the 4170 Å filter. The difference in intensity signals between the G-band and 4170 Å continuum filters is less than 2%. Oscillations with the same period as those previously observed with the G-band filter were observed in the 4170 Å filter area and intensity signals as well. Panel (c) shows the associated IMFs for these three oscillations in the 4170 Å continuum images. Again, black represents the area, and the red curves show the IMFs associated with the intensity signal. The phase relationship observed for these signals is similar to those observed with the G-band continuum images.

images whereby the partially evacuated flux tube allows the observer to see a deeper, hotter region of the photosphere. In G-band, this increase in temperature leads to dissociation of the CH molecule, and therefore the bright points appear brighter (Steiner et al. 2001; Shelyag et al. 2004). Thus, there is a relationship between G-band intensity and temperature, which is necessary for determining the presence of the sausage mode by analyzing the variation of intensity and area signals. This is also seen when comparing the similarities of G-band to other continuum bands (Figure 7).

Due to the fact that more data sets within the ROSA archive employed the G-band filter to observe pores, we decided on using the G-band filter for our analysis to increase the sample size of pores and to remain consistent in our analysis of the pores we had. However, to show conclusively that G-band is an acceptable choice for our analysis, we also analyzed data from another continuum filter (4170 Å with a bandpass of 52 Å) for one of the data sets in our G-band sample. We chose the 2011 December 10 data set, which is shown in the main text. The 4170 Å continuum data set represents the same FOV as the G-band and was operated at the same frame rate. Therefore, the cadence after post facto image reconstruction with the 4170 Å continuum is the same as the G-band (i.e., 2.112 s).

Performing precisely the same analysis as described in Section 4.1 of the main text on the 4170 Å continuum, we find the same oscillations present in the data while analyzing the intensity and area signals (see Figure 7) as we do in G-band. After filtering the data, we also see the same signatures of the surface mode in the 4170 Å continuum as we see in the G-band continuum images. This is, perhaps, unsurprising given that the two filters have similar formation heights (Jess et al. 2010), and the fact that similar oscillations were observed between the two filters has been observed previously for sausage modes in pores (Grant et al. 2015). Furthermore, a study (Jess et al. 2012) of the propagation characteristics of wave phenomena observed between the 4170 Å continuum and the G-band continuum verified that G-band intensities can be matched to density fluctuations. It can be seen from Figure 8 of this study that the *k*-omega diagrams for both bandpasses look identical. This shows that the response of both filters is the same for input wave-like perturbations, and therefore they are both density sensitive. The evidence presented in these studies and with our additional analysis of the 4170 Å continuum data, therefore, gives further credence to the suitability of G-band in studying sausage modes in photospheric pores.

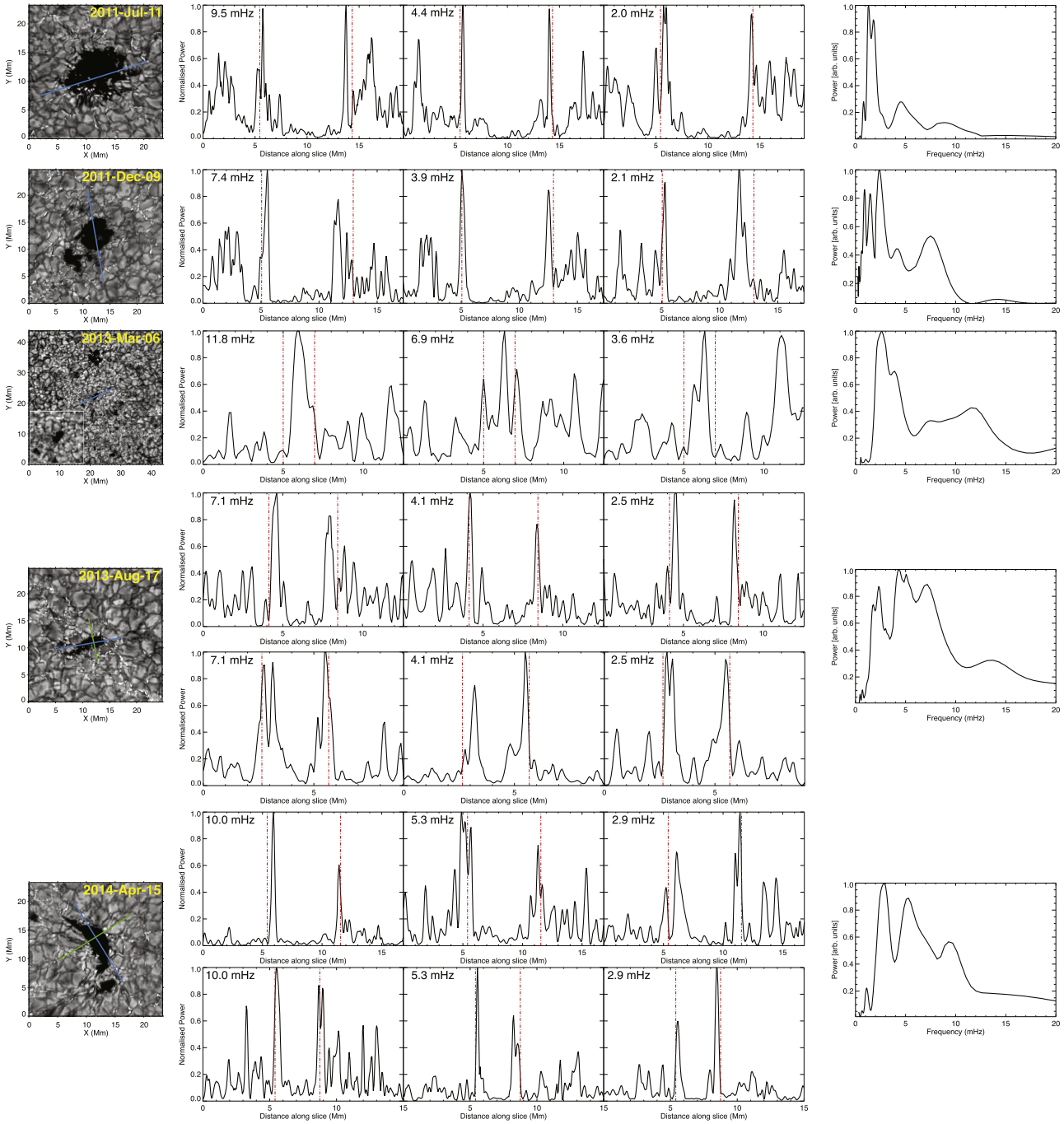

Figure 8. The left column displays a sample view of five further pores analyzed for this study. All images are taken with the G-band filter (4305.5 Å), with yellow labels in the upper right corners indicating the date of observation for the pore. A white box in the 2013 March 06 panel shows a 10 Mm × 10 Mm zoom of the pore under investigation. Blue lines in these images indicate the cross-cuts used to plot the one-dimensional power cross-cuts shown in the plots on the right of each pore. The one-dimensional power cross-cuts for each pore are acquired at the specific dominant oscillation frequencies observed in the data, which have been isolated with a Gaussian filter. In the top left of each cross-cut the labels indicate the central frequency employed in the filter, while the red dashed lines indicate the pore boundary. Peaks at the boundary with a minimum in the center of the pore are a typical feature of the surface mode, while peaks in the center that decay to minima at the boundaries are a characteristic of the body mode. The final two pore images have an additional green line, which indicates an additional set of power cross-cut plots that have been included for these data sets. These cross-cuts are perpendicular to those shown from the blue cross-cut. The upper panels to the right of the pores show the plots for the blue line, while the lower panels show the plots for the green line. The bottom two pore examples are more elliptical in nature than the other pores, and these additional plots have been included to show that the power distribution can be seen at various angles around the pore. The final plots on the far right for each data set show the power as a function of frequency for the pores. The highest power appears within ∼2–5 mHz, which would suggest that *p*-modes are responsible for exciting the waves.

Appendix B
Power Enhancement due to Reconnection

In Section 4.2, it is stated that reconnection may play a role in power enhancement at the pore boundaries. Here we will provide several reasons why we believe that this is not the case in our data, thus strengthening the case for the surface mode. The major tenets of our argument can be summarized as follows:

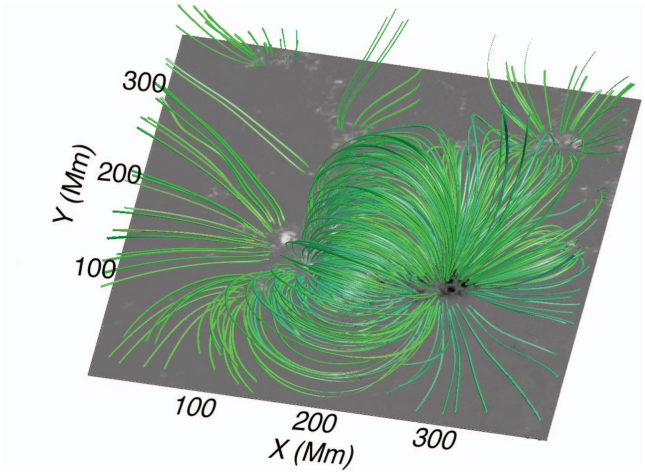

Figure 9. Extrapolated magnetic field lines (green lines) overlaid on the photospheric B_z map from HMI. This corresponds to ROSA data taken on 2011 December 10 shown in the main text, with the center of the image corresponding to the pore under analysis (see lowest image in the stack in Figure 6 of the main text). The box extends to around 110 Mm above the active region. Analyzing the free energies from these extrapolations suggests that reconnection phenomena cannot be responsible for the power enhancement at the pore boundary for our surface mode observations in the filtered data shown in the main text. Therefore, the power enhancements must be the result of wave phenomena observed in the data set.

1. There are few (if any) brightenings at the pore boundary, which could be associated with the reconnection phenomenon.
2. MBP motions do not support large-scale, uniform reconnection about the pore boundary.
3. Analysis of HMI magnetic field data indicates that there is little change in the free energy in the active regions under investigation, indicating that reconnection phenomena are fairly minor in the data.

The first point is that, for reconnection phenomena to be responsible for the power enhancements, it would need to be on a large scale, continuously occurring around the pore boundary. As such, we would expect to observe some form of intensity enhancements around the pore, corresponding to these reconnection events. Within our data sets, however, there are few such intensity enhancements (and in some instances, none at all) around the pore boundary, and definitely not at the scale that would be needed to produce the observed distribution of power. Furthermore, by filtering the data, one could expect that the effects of reconnection would be diminished in the subsequent power plots; however, we still observe the power enhancement around the pore boundary.

As an extension of this point, MBPs (small-scale magnetic elements found in intergranular lanes) do not move in such a way that they could support the uniform reconnection pattern that would be required to produce the power plots that we find in this study. Previous work (Keys et al. 2014) on the 2011 December 10 data analyzed here used a tracking algorithm to study the motion of MBPs in this particular active region. Our study came to the conclusion that the MBPs did not have a preferential direction of motion, that the diffusion of MBPs did not differ between active region MBPs and quiet-Sun MBPs, and that active region MBPs were slightly less dynamic than their quiet-Sun counterparts. This would suggest that reconnection phenomena associated with MBPs drifting near the pore boundary are insufficient to create the power enhancement associated with our surface mode observations.

We can quantify further whether reconnection phenomena are present in the data by employing a nonlinear force-free field extrapolation code (Wiegelmann 2008) on vector magnetograms obtained with HMI. An example of such an extrapolation can be seen in Figure 9 using the 2011 December 10 data. Analyzing the active region as a whole, i.e., including magnetic regions outside our ROSA FOV, we estimate that the free energy (the difference between the nonpotential and potential volume magnetic field energies) decreases by 1.6×10^{27} erg over the course of the data set. However, the estimated 1σ noise threshold is 1.4×10^{29} erg, so the predicted change in free energy is nearly two orders of magnitude below the error estimate of the field energy. The errors associated with the magnetic free energy have been propagated in accordance with Georgoulis & LaBonte (2007), who calculated the relative magnetic helicities and free energies with respect to a potential-field reference, with a detailed analysis of the error calculations presented in Appendix B of Georgoulis et al. (2012). With no macroscopic signatures of (micro)flaring around the pores and minuscule change in the active region's free energy (which is embedded within the noise limit of the extrapolation code), this would suggest that any reconnection phenomenon is exceptionally weak, and not enough to produce the power enhancement in our filtered power plots. Therefore, due to these various reasons, we suggest that the power enhancement we observe is the result of wave phenomena present within the data.

ORCID iDs

Peter H. Keys https://orcid.org/0000-0001-8556-470X
Richard J. Morton https://orcid.org/0000-0001-5678-9002
David B. Jess https://orcid.org/0000-0002-9155-8039
Gary Verth https://orcid.org/0000-0002-9546-2368
Samuel D. T. Grant https://orcid.org/0000-0001-5170-9747
Mihalis Mathioudakis https://orcid.org/0000-0002-7725-6296
Duncan H. Mackay https://orcid.org/0000-0001-6065-8531
Damian J. Christian https://orcid.org/0000-0003-1746-3020
Francis P. Keenan https://orcid.org/0000-0001-5435-1170
Robertus Erdélyi https://orcid.org/0000-0003-3439-4127

References

Aschwanden, M. J., Nakariakov, V. M., & Melnikov, V. F. 2004, ApJ, 600, 458
Banerjee, D., Erdélyi, R., Oliver, R., & O'Shea, E. 2007, SoPh, 246, 3
Beck, C., Bellot Rubio, L. R., Schlichenmaier, R., & Sütterlin, P. 2007, A&A, 472, 607
Bogdan, T. J., & Judge, P. G. 2006, RSPTA, 364, 313
Braun, D. C., Duvall, T. L., Jr., & Labonte, B. J. 1988, ApJ, 335, 1015
De Moortel, I. 2009, SSRv, 149, 65
De Moortel, I., & Nakariakov, V. M. 2012, RSPTA, 370, 3193
De Pontieu, B., Erdélyi, R., & De Moortel, I. 2005, ApJL, 624, L61
De Pontieu, B., Erdélyi, R., & James, S. P. 2004, Natur, 430, 536
Defouw, R. J. 1976, ApJ, 209, 266
Díaz, A. J., & Roberts, B. 2006, A&A, 458, 975
Dorotovič, I., Erdélyi, R., Freij, N., Karlovský, V., & Márquez, I. 2014, A&A, 563, A12
Dorotovič, I., Erdélyi, R., & Karlovský, V. 2008, in IAU Symp. 247, Waves & Oscillations in the Solar Atmosphere: Heating and Magneto-seismology, ed. R. Erdélyi & C. A. Mendoza-Briceno (Cambridge: Cambridge Univ. Press), 351
Dorotovič, I., Rybanský, M., Sobotka, M., et al. 2016, in ASP Conf. Ser. 504, Coimbra Solar Physics Meeting: Ground-based Solar Observations in the

Space Instrumentation Era, ed. I. Dorotovič, C. E. Fischer, & M. Temmer (San Francisco, CA: ASP), 37
Edwin, P. M., & Roberts, B. 1983, SoPh, 88, 179
Erdélyi, R., & Fedun, V. 2010, SoPh, 263, 63
Erdélyi, R., & Morton, R. J. 2009, A&A, 494, 295
Freij, N., Dorotovič, I., Morton, R. J., et al. 2016, ApJ, 817, 44
Freij, N., Scullion, E. M., Nelson, C. J., et al. 2014, ApJ, 791, 61
Georgoulis, M. K., & LaBonte, B. J. 2007, ApJ, 671, 1034
Georgoulis, M. K., Tziotziou, K., & Raouafi, N.-E. 2012, ApJ, 759, 1
Goedbloed, J. P. H., & Poedts, S. (ed.) 2004, Principles of Magnetohydrodynamics (Cambridge: Cambridge Univ. Press)
Grant, S. D. T., Jess, D. B., Moreels, M. G., et al. 2015, ApJ, 806, 132
Grinsted, A., Moore, J. C., & Jevrejeva, S. 2004, NPGeo, 11, 561
Huang, N. E., Shen, Z., Long, S. R., et al. 1998, RSPSA, 454, 903
Huang, N. E., & Wu, Z. 2008, RvGeo, 46, RG2006
Jess, D. B., Mathioudakis, M., Christian, D. J., et al. 2010, SoPh, 261, 363
Jess, D. B., Morton, R. J., Verth, G., et al. 2015, SSRv, 190, 103
Jess, D. B., Shelyag, S., Mathioudakis, M., et al. 2012, ApJ, 746, 183
Keys, P. H., Mathioudakis, M., Jess, D. B., Mackay, D. H., & Keenan, F. P. 2014, A&A, 566, A99
Li, W., Ai, G., & Wang, H. 2001, PBeiO, 37, 15
Ludwig, H.-G., Samadi, R., Steffen, M., et al. 2009, A&A, 506, 167
Luna-Cardozo, M., Verth, G., & Erdélyi, R. 2012, ApJ, 748, 110
Maltby, P., Avrett, E. H., Carlsson, M., et al. 1986, ApJ, 306, 284
Mathioudakis, M., Jess, D. B., & Erdélyi, R. 2013, SSRv, 175, 1
Moreels, M. G., Freij, N., Erdélyi, R., Van Doorsselaere, T., & Verth, G. 2015a, A&A, 579, A73
Moreels, M. G., Goossens, M., & Van Doorsselaere, T. 2013, A&A, 555, A75
Moreels, M. G., Van Doorsselaere, T., Grant, S. D. T., Jess, D. B., & Goossens, M. 2015b, A&A, 578, A60
Morton, R. J., Erdélyi, R., Jess, D. B., & Mathioudakis, M. 2011, ApJL, 729, L18
Morton, R. J., Tomczyk, S., & Pinto, R. 2015, NatCo, 6, 7813
Morton, R. J., Verth, G., Jess, D. B., et al. 2012, NatCo, 3, 1315
Nakariakov, V. M., & Verwichte, E. 2005, LRSP, 2, 3
Pesnell, W. D., Thompson, B. J., & Chamberlin, P. C. 2012, SoPh, 275, 3
Rae, I. C., & Roberts, B. 1983, SoPh, 84, 99
Rimmele, T. R. 2004, Proc. SPIE, 5490, 34
Roberts, B., & Webb, A. R. 1978, SoPh, 56, 5
Rouppe van der Voort, L. H. M., Rutten, R. J., Sütterlin, P., Sloover, P. J., & Krijger, J. M. 2003, A&A, 403, 277
Sakurai, T., Goossens, M., & Hollweg, J. V. 1991, SoPh, 133, 247
Schou, J., Borrero, J. M., Norton, A. A., et al. 2012, SoPh, 275, 327
Shelyag, S., Schüssler, M., Solanki, S. K., Berdyugina, S. V., & Vögler, A. 2004, A&A, 427, 335
Sobotka, M. 2003, AN, 324, 369
Spruit, H. C. 1982, SoPh, 75, 3
Steiner, O., Hauschildt, P. H., & Bruls, J. 2001, A&A, 372, L13
Sütterlin, P., Schröter, E. H., & Muglach, K. 1996, SoPh, 164, 311
Terradas, J., Oliver, R., & Ballester, J. L. 2004, ApJ, 614, 435
Torrence, C., & Compo, G. P. 1998, BAMS, 79, 61
Verma, M., & Denker, C. 2014, A&A, 563, A112
Vernazza, J. E., Avrett, E. H., & Loeser, R. 1981, ApJS, 45, 635
Wang, T. 2011, SSRv, 158, 397
Wiegelmann, T. 2008, JGRA, 113, A03S02
Wöger, F., von der Lühe, O., & Reardon, K. 2008, A&A, 488, 375
Yu, D. J., Van Doorsselaere, T., & Goossens, M. 2017a, A&A, 602, A108
Yu, D. J., Van Doorsselaere, T., & Goossens, M. 2017b, ApJ, 850, 44
Zhugzhda, Y. D., Balthasar, H., & Staude, J. 2000, A&A, 355, 347